Acta Geotechnica (2022) 17:2783–2798
https://doi.org/10.1007/s11440-021-01362-y

RESEARCH PAPER

# Correlation between grain shape and critical state characteristics of uniformly graded sands: A 3D DEM study

Jia-Yan Nie[1,2] · Jidong Zhao[3] · Yi-Fei Cui[1] · Dian-Qing Li[2]

Received: 28 December 2020 / Accepted: 17 September 2021 / Published online: 16 October 2021
© The Author(s), under exclusive licence to Springer-Verlag GmbH Germany, part of Springer Nature 2021

## Abstract

The multi-scale characteristics of particle morphology, including the overall form, local roundness and surface roughness, affect the critical state behavior of sands and should be considered in modern critical state-based continuum constitutive modeling. Despite extensive experimental and numerical studies, no consensus has been reached as to how particle morphology may quantitatively dictate the critical state response of sands. This study presents a numerical investigation based on discrete element method (DEM) in an attempt to address this outstanding issue. Five DEM samples of uniformly graded sands consisting of realistic shape clumps and ideal spheres of different mass proportions are prepared and subjected to conventional drained and undrained triaxial compression under different initial void ratios and stress states. A 3D overall regularity (*OR*) index is adopted to quantify both the overall form and local roundness characteristics of these assemblies. It is shown that this shape parameter *OR* may effectively help to elucidate the correlation between mechanical properties, especially the critical state behavior of sand and particle shape, and has a great potential for incorporation into the framework of anisotropic critical state theory for constitutive modeling of sand behavior. The study helps to advance our cross-scale understanding of microscopic grain-scale morphology information in relation to macroscopic soil behavior.

**Keywords** Anisotropic critical state theory · DEM · Overall regularity · Particle morphology · Sands

## 1 Introduction

Granular materials such as sands behave differently from continuum media when subjected to external loading and may exhibit many salient features such as stress dilatancy, anisotropy, state dependence and nonlinear elasticity [2, 3, 7, 21, 25], among which critical state behavior is one of the most important mechanical responses of sands, which represents the ultimate state for soils under sustained shearing. The classic critical sate theory (CST) holds that the soil deformation will reach a final state of shear failure, termed as critical state or steady state, at which the soil deforms continuously under constant stress and volume conditions [6, 36, 39, 46]. This pioneering theory links the soil strength and deformation and lays a solid foundation for constitutive modeling of soil behaviors. In the past decade, with the increasing knowledge of the sand behaviors especially of its micromechanical behaviors, an elegant anisotropic critical state theory (ACST) had been presented by Li and Dafalias [20] from the perspective of thermo-dynamical principles and DEM observations. The

✉ Yi-Fei Cui
yifeicui@mail.tsinghua.edu.cn

Jia-Yan Nie
njiayan@mail.tsinghua.edu.cn

Jidong Zhao
jzhao@ust.hk

Dian-Qing Li
dianqing@whu.edu.cn

[1] State Key Laboratory of Hydroscience and Engineering, Tsinghua University, Beijing 100084, People's Republic of China

[2] State Key Laboratory of Water Resources and Hydropower Engineering Science, Institute of Engineering Risk and Disaster Prevention, Wuhan University, Wuhan 430072, People's Republic of China

[3] Department of Civil and Environmental Engineering, The Hong Kong University of Science & Technology, Clear Water Bay, Kowloon, Hong Kong, People's Republic of China

ACST enhanced the traditional CST by imposing an additional condition that soil fabric should satisfy at the critical state and showed that the norm of the developed deviatoric fabric tensor would reach a unique value that depended on the loading path, while the direction of that would evolve toward the loading direction. Zhao and Guo [56] further identified a unique property associated with the fabric structure relative to the stresses at critical state based on DEM simulations with sphere particles under different shear modes, and found that the first joint invariant of the deviatoric stress and fabric tensors was path-independent. Yang and Wu [52] also found that a simple normalization of the contact normal-based fabric tensor by the specific volume of the sample leaded to a unique representation of fabric anisotropy at the critical state for non-sphere specimens. These significant improvements of CSL promoted the occurrence of a series of constitutive modelings considering soil fabric anisotropy (e.g., [12–14, 44, 59]), which rendered the continuum theories physically more robust and their predictions of soil behaviors are more consistent with field observations. However, an outstanding challenge any constitutive modeling modeler has to face is that the increasing number of constitutive parameters increases the difficulties of model calibration due to the assumed parameters with no clear physical meanings (e.g., [59, 60]). Hence, it is necessary to explore the micro-mechanical origins of these macro-mechanical behaviors and build an explicit relationship between constitutive parameters and particle scale properties in order to relieve the calibration work and make the constitutive models more physical.

The complex macro-mechanical behaviors of sands mainly originate from the packing patterns and interactions of the constituent particles and are further related to the particle basic characteristics (e.g., particle size, particle size distribution, particle morphology, mineralogy, etc.) [8, 9, 11, 19, 24, 38, 49], among which the effect of particle morphology on critical state behaviors of sands has been extensively studied by experimental and numerical methods, especially the DEM due to its easy maneuverability for soil element tests approaching critical state. Firstly, different aspects of particle shape have been found to affect the critical state shearing resistance significantly, including aspect ratio, angularity, nonconvexity, sphericity and rolling friction [1, 4, 5, 32, 35, 57]. Yang and Luo [50] further found that the critical state lines (CSLs) in both *e-p'* and *q-p'* planes were affected obviously by particle shape, and the slop and intercept of the CSL in *e-p'* space increase with the particle overall irregularity. However, Xie et al. [47] and Jiang et al. [18] found that particle aspect ratio had a negligible effect on the CSL in *e-p'* plane based on DEM simulations using simple clumps with varying aspect ratios. Nguyen et al. [28] came to a similar conclusion that the critical state data points for spheres and ellipsoids were plotted on almost the same CSLs in *e-p'* plane, whereas the CSLs of clumps with different degrees of eccentricity were plotted above them. Xu et al. [48] used more complex shaped particles to conduct DEM simulations and found that particle irregularity positively affected both the absolute slope and the intercept of the CSL in the *e-p'* plane. In addition, the unique normalized contact normal-based fabric norms were observed in Xie et al. [47], Jiang et al. [18] and Xu et al. [48] for granular samples consisting of non-sphere particles at the critical state, respectively. Motivated by these findings, quantitative relations between critical state parameters and particle shape descriptors have been established under the CST framework. For example, Yang and Luo [50] conducted experimental tests to build correlations between critical state parameters and particle overall regularity and roundness. Nguyen et al. [28] explored relations between critical state parameters, dilatancy parameters and particle sphericity through DEM simulations on four samples consisting of spheres, ellipsoids and two other simple clumps. Nguyen et al. [29] further incorporated particle sphericity into the SANISAND constitutive model to predict the undrained and drained DEM responses of these four numerical samples. However, 2D shape parameters are often adopted in the laboratory based on the QICPIC apparatus, and simple particle geometries are used in previous DEM studies when building these relations. These simplifications may not be representative for the realistic particle shape characteristics of granular soils (e.g., 3D shape features and shape polydispersity). Hence, more realistic shape particles need to be considered in DEM simulations to examine their effects on the macro- and micro-mechanical responses of granular sands, especially the critical state fabric characteristics under the framework of ACST.

Therefore, in this study, five types of granular assemblies with different particle shape characteristics are prepared in DEM to conduct conventional drained and undrained triaxial compression simulations under different initial stress and density states, in order to give more insights into the effect of particle morphology on behaviors of sands, especially the critical state behavior. A 3D particle overall regularity index is adopted to quantify the overall particle shape characteristic of soil sample more reasonably. And this shape index is further used to correlate critical state parameters and particle shape characteristics of granular soils. This paper is organized as follows: Firstly, the numerical modeling programs and procedure and also the definitions of some concerned macro- and micro-mechanical quantities are firstly presented, and then, the typical macroscopic and microscopic simulation results are analyzed. In the following, the influence of particle overall regularity on the critical state properties of sands, and also the relations between overall regularity and

critical state parameters are discussed. Based on these results, the conclusions are finally given.

## 2 Numerical tests

### 2.1 Numerical program and procedure

In order to consider more realistic shape particles in DEM, complex clumps are used in this study to approximate the sand particles. According to our previous proposed framework of DEM simulation considering realistic particle shape and grading characteristics based on a limited number of X-ray CT scanned particles [30, 31], 5000 virtual Leighton Buzzard sand (LBS) particles are generated randomly as clump templates to create complex clumps using the 'Bubble Packing' algorithm in DEM commercial software PFC$^{3D}$ [41]. Figure 1(a) gives the corresponding clumps within a virtual triaxial shear apparatus adopted in this study and one typical LBS clump, which is generated by the minimum particle size ratio of $q_r = 0.5$ and sphere–sphere intersection angle of $u = 150°$. To quantitatively describe the shape and size poly-dispersity of these distinct clumps, the common particle size and shape parameters, including equi-voluminal sphere diameter (*ESD*), aspect ratio (*AR*), sphericity (*S*) and convexity (*C*), are accurately analyzed for each clump, according to the corresponding definitions [45, 54, 58], which are also illustrated in Fig. 1(a). The surface meshing method is used to calculate three principal dimensions ($P_1$, $P_2$, $P_3$) and convex hull volumes ($V_{ch}$) of these clumps, which can acquire a high accuracy when the surface mesh size is small enough. However, due to the smooth surface characteristics of clump particles, the calculated surface area based on surface meshing method may be much larger than the real value despite the very small surface mesh size. Therefore, a Monte Carlo method is adopted here to compute the surface area (*SA*) and volume (*V*) of each clump. Figure 1(b) and Fig. 1(c) gives the empirical cumulative distribution functions (CDFs) of these particle size and shape parameters, respectively, and the representative particle size and shape index of $ESD_{50}$, $AR_s$, $S_s$ and $C_s$ corresponding to 50% cumulative probability distribution are 1.96 mm, 0.844, 0.916 and 0.929, respectively. And the coefficient of uniformity, $C_u$, of these clumps based on *ESD* is about 1.27, which suggests that this virtual specimen consisting of these complex clumps can be able to represent a type of uniformly graded sandy soil consisting of sub-rounded particles.

The simple liner contact model is adopted in this study to ensure the computation efficiency. Table 1 summarizes the model parameters of the simulation according to our previous study [30, 31]. To account for the influence of particle shape on the critical state properties, five different mass proportions of clumps and spheres are mixed together to prepare granular assemblies with different particle overall irregularities. And then, the corresponding drained and undrained triaxial compression simulations are conducted under different initial stress and density states. To be specific, 5000 distinct clumps with no contacts between

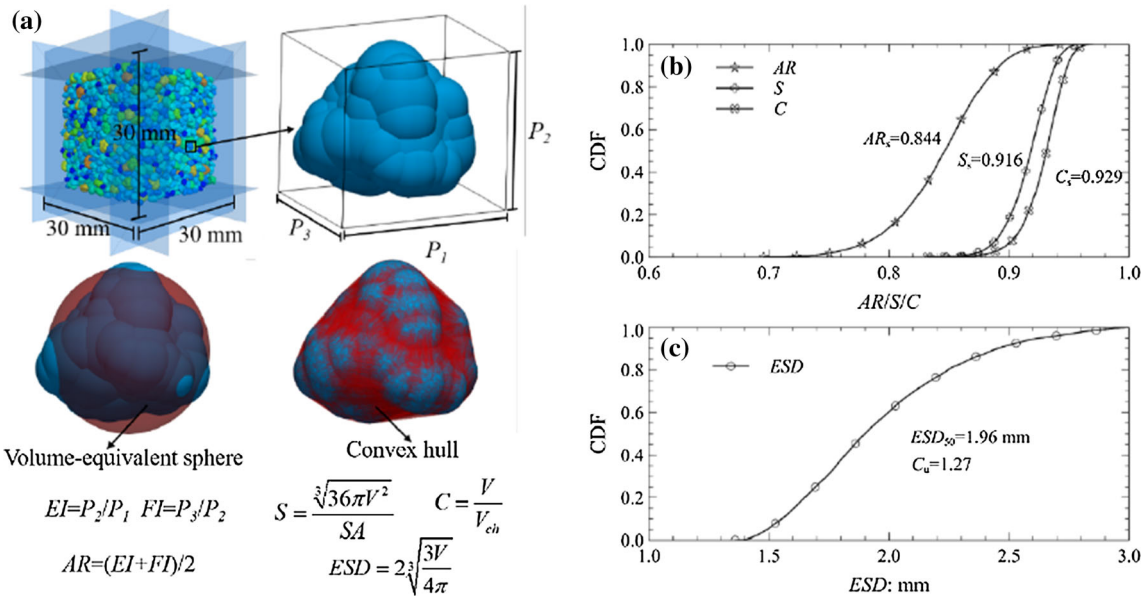


**Fig. 1** a Numerical model configuration, typical clump and the illustration of its shape parameters: *ESD*: equi-voluminal sphere diameter; *AR*: aspect ratio; *S*: sphericity; *C*: convexity; $P_1$: the first principal dimension; $P_2$: the second principal dimension; $P_3$: the third principal dimension; *EI*: elongation index; *FI*: flat index; *V*: particle volume; *SA*: particle surface area; $V_{ch}$: convex hull volume; b empirical CDFs of *AR*, *S* and *C*; c empirical CDFs of *ESD* (Modified from Nie et al. [30])

**Table 1** DEM parameters adopted for triaxial compression simulations

| Parameters | Values |
|---|---|
| Particle density, q ($10^4$ kg/m$^3$) | 2650 |
| Inter-particle friction during compression, l | 0.3 |
| Wall-particle friction | 0.0 |
| Damping coefficient, $a$ | 0.3 |
| Inter-particle normal contact stiffness, $k_n/r^*$ (MPa) | 100 |
| Inter-particle shear contact stiffness, $k_s/r^*$ (MPa) | 100 |
| Wall-particle normal contact stiffness ($N$/m) | 1.0 9 $10^7$ |

$r*$ refers to the average equi-voluminal sphere radius of the particle assemblies

each other are firstly incorporated into a large smooth cubic triaxial compression box and then randomly replaced by a certain number of equi-voluminal spheres (e.g., 0, 1250, 2500, 3750, 5000) to make five specimens with varying particle overall irregularities but same grading characteristics. The corresponding mass proportions of ideal spheres within these five assemblies are 0, 25.2%, 50.1%, 74.5% and 100%, respectively. And then a numerical stress servo-control algorithm is adopted to compress the specimen isotropically to the desired initial stress state until reaching an equilibrium state. During this process, different inter-particle friction coefficients can be assigned onto particles in order to acquire samples with different initial densities. The isotropic compression stage is terminated when the unbalanced force ratio is less than $10^{-5}$, which indicates that the sample has already reached a mechanically stable state. For the convenience of results analysis, five well-'consolidated' specimens are named as S0GB100, S25GB75, S50GB50, S75GB25 and S100GB0, respectively, where 'S' represents sand and 'GB' represents glass beads from the perspective of simulated materials, and the numbers following are the corresponding rounding mass proportions.

After the 'consolidation' process simulation, the inter-particle friction is restored to a typical value of quartz sand particle, 0.3, and the particle surface friction herein represents the roughness effect on the sand behavior. In the following, conventional drained and undrained triaxial compression tests are simulated based on constant stress and constant volume servo-control mechanism, respectively. To be specific, during shearing, a numerical stress servo scheme is used to constantly adjust the positions of lateral four confining walls according to the evolutions of contact forces on these walls to ensure that the confining pressure is kept at 100 kPa. And a numerical volume servo scheme is adopted to continually adjust the positions of lateral four confining walls according to the evolutions of the axial strain to keep the sample volume constant. A relatively small loading rate 0.01/$s$ is adopted to compress the sample in order to ensure a quasi-static shearing. And the inertial number ($I = \underline{c}d=^{p}$ $P$=q) is always lower than 0.001 during the whole shearing process [23], where $\underline{c}$ is the strain rate, $d$ is the average particle diameter, $P$ is the confining pressure and q is the particle density. The triaxial compression simulations are stopped when an obvious critical state behavior is observed under both drained and undrained conditions. Specifically, the drained shearing and undrained shearing simulations are stopped at the axial strain of 40% and 60%, respectively. It should be noted that particle density scaling strategy with a multiplying factor of $10^4$ is adopted in this study to acquire a relative acceptable critical time step in order to reduce the computation burden reference to O'Sullivan [33]. And the actual computational time step is set to $10^{-5}$ s for all simulations, less than the critical time step. Thornton and Antony [43] had noted that this method had a negligible effect on the contact forces and displacements of particles within the sample and hence the stress and strain of the sample under the quasi-static condition.

In order to quantify the shape differences of these five granular assemblies, the 3D overall regularity ($OR$) proposed by Yang and Luo [50] is referenced in this study, which is determined by the following expressions:

$$OR = (AR_c + S_c + C_c)=3 \tag{1}$$

$$AR_c = AR_S \times x_S + AR_{GB} \times x_{GB} \tag{2}$$

$$S_c = S_S \times x_S + S_{GB} \times x_{GB} \tag{3}$$

$$C_c = C_S \times x_S + C_{GB} \times x_{GB} \tag{4}$$

where $AR_S$, $S_S$ and $C_S$ are the representative values of aspect ratio, sphericity and convexity of LBS clumps corresponding to 50% cumulative probability distribution, respectively. Similarly, $AR_{GB}$, $S_{GB}$ and $C_{GB}$ are the corresponding indices for ideal spheres, and herein, they are both 1.0. $x_S$ and $x_{GB}$ are the mass proportion of LBS clumps and ideal spheres, respectively. $AR_c$, $S_c$ and $C_c$ are the combined aspect ratio, sphericity and convexity of the granular assembly, respectively. Table 2 summarizes the particle size and shape parameters of these five different types of granular assemblies.

In this study, different inter-particle friction angles are adopted during the isotropic consolidation process to make samples before shearing with different initial densities under different stress states. Table 3 summarizes all simulation programs in this study, and the simulation program ID is defined according to the naming format of 'SNDCN,' where 'SN' represents the specimen name in Table 2; 'DC' indicates the drainage condition during the shearing process and can be 'D' and 'UD' for drained and undrained,

**Table 2** Particle size and shape parameters of the five granular assemblies

| Specimens | $C_u$ | $ESD_{50}$: mm | $AR_c$ | $S_c$ | $C_c$ | $OR$ |
|---|---|---|---|---|---|---|
| S0GB100 | 1.27 | 1.96 | 1.000 | 1.000 | 1.000 | 1.000 |
| S25GB75 | 1.27 | 1.96 | 0.960 | 0.979 | 0.982 | 0.974 |
| S50GB50 | 1.27 | 1.96 | 0.922 | 0.958 | 0.965 | 0.948 |
| S75GB25 | 1.27 | 1.96 | 0.883 | 0.937 | 0.947 | 0.922 |
| S100GB0 | 1.27 | 1.96 | 0.844 | 0.916 | 0.929 | 0.896 |

$C_u$: the uniformity coefficient, $ESD_{50}$: the equi-voluminal sphere diameter corresponding to 50% cumulative probability distribution; $AR_c$: the combined aspect ratio, $S_c$: the combined sphericity, $C_c$: the combined convexity; $OR$: the combined overall regularity

respectively; 'N' is the simulation ID. There are at least 15 simulation cases for each type of granular assemblies with varying $OR$s in order to ensure that the critical state properties acquired in this study are reliable and convincing.

## 2.2 Definitions of macro- and micro-mechanical quantities

The most attractive benefit of DEM to geotechnical engineering community is that it cannot only acquire common macro-mechanical quantities (e.g., stress and strain) but also microscopic quantities (e.g., coordination number and anisotropic fabric) within soils, which promotes the understanding of soil behaviors from the perspective of micromechanics. In this section, the definitions of primary macro- and micro-mechanical quantities used in triaxial compression behaviors analysis of granular soils are introduced briefly for completeness.

### 2.2.1 Stress and strain

The stress tensor $\mathsf{r}_{ij}$ within the assembly is derived through the definition proposed by Christoffersen et al. [10]:

$$\mathsf{r}_{ij} = \frac{1}{V}\sum_{c\in V} f_i^c d_j^c \tag{5}$$

where $V$ is the volume of the assembly; $f_i^c$ is the $i$-th component of contact force vector $\mathsf{f}$ at the contact $c$; $d_j^c$ is the $j$-th component of branch vector $\mathsf{d}$ joining the mass centers of the two contacting particles at the contact $c$. And then the effective mean stress $p'$ and deviatoric stress $q$ can be defined as follows:

$$p' = \frac{1}{3}\mathsf{r}_{ii} \tag{6}$$

$$q = \sqrt{\frac{3}{2}\mathsf{r}'_{ij}\mathsf{r}'_{ij}} \tag{7}$$

where $\mathsf{r}'_{ij}$ is the deviatoric part of stress tensor $\mathsf{r}_{ij}$, i.e., $\mathsf{r}'_{ij} = \mathsf{r}_{ij} - p'\mathsf{d}_{ij}$ and $\mathsf{d}_{ij}$ is the Kronecker delta tensor.

In addition, the excess pore water pressure, $u$, within the assembly under the undrained shearing condition (constant volume test simulations) can be indirectly derived from the reduction between the current $p'$ and the initial effective mean stress $p'_0$ in constant volume test reference to Sitharam et al. [40].

For the strain measurement, the axial strain $\mathsf{e}_1$ and volumetric strain $\mathsf{e}_v$ can be determined based on the displacements of the boundary walls and volume change of the assembly according to the following equations:

$$\mathsf{e}_1 = -\int_{H_0}^{H}\frac{1}{h}\,dh = \ln\frac{H_0}{H} \tag{8}$$

$$\mathsf{e}_v = \mathsf{e}_1 + \mathsf{e}_2 + \mathsf{e}_3 = -\int_{V_0}^{V}\frac{1}{V}\,dv = \ln\frac{V_0}{V} \tag{9}$$

where $H_0$ and $V_0$ are the initial height and volume of the well-'consolidated' packing before shearing, respectively, and $H$ and $V$ are the height and volume of the deformed packing during shearing, respectively. A positive value of the volumetric strain $\mathsf{e}_v$ represents compression in this study following the convention of soil mechanics.

### 2.2.2 Coordination number and anisotropic fabric

There are mainly two types of coordination numbers encountered in the literature in order to quantify the contact density within the assembly, named mean coordination number $CN$ and mechanical coordination number $Z_m$, which is defined by Rothenburg and Bathurst [37] and Thornton [42], respectively, as follows:

$$CN = 2C/N \tag{10}$$

$$Z_m = (2C - N_1)/(N - N_1 - N_0) \tag{11}$$

where $C$ is the total number of contacts within the assembly, and $N$ is the number of particles, $N_1$ and $N_0$ are the numbers of particles having only one and zero contact in the specimen, respectively. Note that the evolutions of both parameters are almost parallel during triaxial shearing; hence, only mechanical coordination number is discussed in this study since it is more directly related to the mechanical stability of granular materials.

The scalar coordination number reflects the internal fabric structure of the granular assembly to some extent and is very closely related to the mechanical stability of the sample. Nonetheless, many studies have reported that the soil fabric is highly anisotropic during shearing; hence, a deviatoric second-order fabric tensor $\mathsf{F}$ based on the

**Table 3** Simulation programs and critical state quantities of triaxial compression tests

| Test ID | $p'_0$(kPa) | $e_0$ | $e_c$ | $p'_c$ | $q_c$ (kPa) | $K_c$ (kPa) |
|---|---|---|---|---|---|---|
| S0GB100D0 | 25 | 0.622 | 0.722 | 37.7 | 29.8 | 11.0 |
| S0GB100D1 | 50 | 0.616 | 0.718 | 70.5 | 52.9 | 20.4 |
| S0GB100D2 | 75 | 0.614 | 0.715 | 103.0 | 75.8 | 29.7 |
| S0GB100D3 | 100 | 0.610 | 0.709 | 135.3 | 97.5 | 35.3 |
| S0GB100D4 | 150 | 0.600 | 0.706 | 199.5 | 139.9 | 51.1 |
| S0GB100D5 | 200 | 0.595 | 0.699 | 265.7 | 188.3 | 68.6 |
| S0GB100D6 | 300 | 0.583 | 0.686 | 396.6 | 280.9 | 98.7 |
| S0GB100D7 | 400 | 0.574 | 0.666 | 535.6 | 396.8 | 138.0 |
| S0GB100D8 | 600 | 0.552 | 0.643 | 791.6 | 565.0 | 185.3 |
| S0GB100D9 | 800 | 0.536 | 0.618 | 1055.5 | 756.3 | 239.3 |
| S0GB100UD1 | 50 | 0.616 | 0.616 | 1145.1 | 821.8 | 248.7 |
| S0GB100UD2 | 100 | 0.610 | 0.610 | 1212.0 | 866.8 | 262.9 |
| S0GB100UD3 | 200 | 0.595 | 0.595 | 1398.7 | 1018.0 | 308.7 |
| S0GB100UD4 | 400 | 0.574 | 0.574 | 1630.0 | 1184.6 | 347.1 |
| S0GB100UD5 | 800 | 0.536 | 0.536 | 2112.0 | 1498.6 | 400.8 |
| S0GB100UD6 | 100 | 0.727 | — | — | — | — |
| S25GB75D0 | 25 | 0.619 | 0.752 | 39.0 | 35.2 | 19.3 |
| S25GB75D1 | 50 | 0.613 | 0.754 | 73.9 | 64.6 | 37.4 |
| S25GB75D2 | 75 | 0.610 | 0.749 | 107.5 | 90.8 | 51.4 |
| S25GB75D3 | 100 | 0.607 | 0.745 | 141.9 | 119.3 | 70.3 |
| S25GB75D4 | 150 | 0.601 | 0.744 | 209.9 | 173.1 | 101.2 |
| S25GB75D5 | 200 | 0.595 | 0.733 | 279.9 | 233.8 | 134.6 |
| S25GB75D6 | 300 | 0.584 | 0.721 | 419.0 | 351.3 | 212.2 |
| S25GB75D7 | 400 | 0.577 | 0.707 | 554.5 | 459.4 | 262.8 |
| S25GB75D8 | 600 | 0.558 | 0.684 | 827.3 | 678.1 | 412.6 |
| S25GB75D9 | 800 | 0.546 | 0.666 | 1097.4 | 889.5 | 531.7 |
| S25GB75UD1 | 50 | 0.613 | 0.613 | 1871.9 | 1496.3 | 906.1 |
| S25GB75UD2 | 100 | 0.607 | 0.607 | 1927.2 | 1562.1 | 972.5 |
| S25GB75UD3 | 200 | 0.595 | 0.595 | 2186.4 | 1810.7 | 1117.0 |
| S25GB75UD4 | 400 | 0.577 | 0.577 | 2465.7 | 1995.8 | 1247.1 |
| S25GB75UD5 | 800 | 0.546 | 0.546 | 3048.7 | 2425.0 | 1460.7 |
| S25GB75UD6 | 100 | 0.757 | — | — | — | — |
| S25GB75UD7 | 800 | 0.641 | 0.641 | 1545.7 | 1247.1 | 776.0 |
| S25GB75UD8 | 100 | 0.655 | 0.655 | 1321.5 | 1068.7 | 662.4 |
| S50GB50D0 | 25 | 0.618 | 0.784 | 41.5 | 42.3 | 29.5 |
| S50GB50D1 | 50 | 0.616 | 0.786 | 76.6 | 73.4 | 51.2 |
| S50GB50D2 | 75 | 0.608 | 0.781 | 113.2 | 107.6 | 78.7 |
| S50GB50D3 | 100 | 0.611 | 0.779 | 147.5 | 136.7 | 98.4 |
| S50GB50D4 | 150 | 0.602 | 0.773 | 219.0 | 201.2 | 148.0 |
| S50GB50D5 | 200 | 0.600 | 0.771 | 290.7 | 267.2 | 198.4 |
| S50GB50D6 | 300 | 0.588 | 0.759 | 434.8 | 399.6 | 301.1 |
| S50GB50D7 | 400 | 0.584 | 0.746 | 584.4 | 550.0 | 435.8 |
| S50GB50D8 | 600 | 0.566 | 0.729 | 856.6 | 767.2 | 587.4 |
| S50GB50D9 | 800 | 0.558 | 0.706 | 1140.6 | 1023.1 | 821.0 |
| S50GB50UD1 | 50 | 0.616 | 0.616 | 3059.8 | 2650.4 | 2097.4 |
| S50GB50UD2 | 100 | 0.611 | 0.611 | 3229.6 | 2790.5 | 2215.8 |
| S50GB50UD3 | 200 | 0.600 | 0.600 | 3521.3 | 3034.6 | 2387.9 |
| S50GB50UD4 | 800 | 0.665 | 0.665 | 2032.5 | 1772.1 | 1380.3 |

**Table 3** (continued)

| Test ID | $p'_0$(kPa) | $e_0$ | $e_c$ | $p'_c$ | $q_c$ (kPa) | $K_c$ (kPa) |
|---|---|---|---|---|---|---|
| S50GB50UD5 | 100 | 0.700 | 0.700 | 1426.2 | 1278.6 | 1017.3 |
| S50GB50UD6 | 100 | 0.762 | 0.762 | 400.5 | 354.9 | 265.6 |
| S50GB50UD7 | 200 | 0.690 | 0.690 | 1603.9 | 1429.5 | 1126.4 |
| S50GB50UD8 | 400 | 0.673 | 0.673 | 1841.5 | 1600.0 | 1236.4 |
| S50GB50UD9 | 800 | 0.645 | 0.645 | 2400.9 | 2117.1 | 1697.3 |
| S75GB25D0 | 25 | 0.625 | 0.825 | 44.3 | 49.7 | 40.5 |
| S75GB25D1 | 50 | 0.623 | 0.825 | 81.9 | 87.7 | 72.1 |
| S75GB25D2 | 75 | 0.621 | 0.819 | 119.4 | 125.4 | 106.0 |
| S75GB25D3 | 100 | 0.618 | 0.818 | 158.0 | 167.2 | 149.3 |
| S75GB25D4 | 150 | 0.612 | 0.809 | 231.0 | 236.6 | 203.8 |
| S75GB25D5 | 200 | 0.609 | 0.807 | 308.6 | 319.5 | 288.0 |
| S75GB25D6 | 300 | 0.599 | 0.798 | 451.7 | 451.1 | 401.1 |
| S75GB25D7 | 400 | 0.593 | 0.785 | 596.8 | 588.3 | 517.9 |
| S75GB25D8 | 600 | 0.582 | 0.762 | 910.6 | 931.1 | 2305.5 |
| S75GB25D9 | 800 | 0.571 | 0.747 | 1197.4 | 1197.1 | 1088.0 |
| S75GB25UD1 | 200 | 0.744 | 0.744 | 1506.6 | 1449.1 | 1339.9 |
| S75GB25UD2 | 400 | 0.728 | 0.728 | 1928.9 | 1837.6 | 1725.3 |
| S75GB25UD3 | 800 | 0.703 | 0.703 | 2607.5 | 2473.6 | 2305.5 |
| S75GB25UD4 | 50 | 0.685 | 0.685 | 3022.4 | 2852.6 | 2682.9 |
| S75GB25UD5 | 200 | 0.671 | 0.671 | 3544.7 | 3299.8 | 3062.0 |
| S75GB25UD6 | 100 | 0.757 | 0.757 | 1220.5 | 1166.1 | 1061.6 |
| S100GB0D0 | 25 | 0.637 | 0.869 | 44.8 | 52.7 | 49.4 |
| S100GB0D1 | 50 | 0.635 | 0.862 | 85.6 | 99.2 | 95.6 |
| S100GB0D2 | 75 | 0.633 | 0.858 | 124.2 | 141.5 | 137.8 |
| S100GB0D3 | 100 | 0.631 | 0.856 | 163.3 | 183.5 | 182.2 |
| S100GB0D4 | 150 | 0.627 | 0.849 | 240.2 | 265.0 | 264.2 |
| S100GB0D5 | 200 | 0.625 | 0.847 | 320.2 | 355.7 | 366.2 |
| S100GB0D6 | 300 | 0.618 | 0.829 | 470.9 | 509.4 | 518.3 |
| S100GB0D7 | 400 | 0.612 | 0.822 | 630.1 | 689.4 | 716.9 |
| S100GB0D8 | 600 | 0.600 | 0.811 | 926.9 | 984.0 | 1020.7 |
| S100GB0D9 | 800 | 0.591 | 0.796 | 1235.5 | 1314.3 | 1388.1 |
| S100GB0UD1 | 50 | 0.784 | 0.784 | 1809.4 | 1856.6 | 1921.0 |
| S100GB0UD2 | 100 | 0.780 | 0.780 | 1872.7 | 1864.2 | 1903.3 |
| S100GB0UD3 | 200 | 0.771 | 0.771 | 2200.5 | 2239.5 | 2349.3 |
| S100GB0UD4 | 400 | 0.758 | 0.758 | 2623.9 | 2615.0 | 2679.3 |
| S100GB0UD5 | 800 | 0.735 | 0.735 | 3454.7 | 3436.7 | 3474.9 |
| S100GB0UD6 | 100 | 0.761 | 0.761 | 2571.2 | 2594.0 | 2672.1 |

*TEST ID: SNDCN, where 'SN' represents the specimen name in Table 2, 'DC' indicates the drainage condition, 'N' is the simulation ID, and '—' means that the specimen experiences static liquefaction during the numerical test

contact normal is often adopted to characterize this anisotropic microstructure, which is defined as [56]:

$$\mathbf{F} = (\mathbf{G} - \frac{1}{3}\mathbf{I}) \; with \; \mathbf{G} = \frac{1}{N}\sum_{k=1}^{N} (\mathbf{l}^k \otimes \mathbf{l}^k) \tag{12}$$

where $N$ is the total number of contacts within the assembly; $l^k$ is the unit contact normal vector of the $k$th contact; $\mathbf{I}$ is the unit tensor. As a deviatoric tensor, the two invariants, i.e., the norm of $\mathbf{F}$, $F$ and also the unit direction $\mathbf{n}_F$, satisfy the following relations [47]:

$$\mathbf{F} = F\mathbf{n}_F \; with \; F = \sqrt{\mathbf{F} : \mathbf{F}}; \; \mathbf{n}_F : \mathbf{n}_F = 1; \; tr\mathbf{n}_F = 0 \tag{13}$$

where the unit direction $\mathbf{n}_F$ represents the direction of the deviatoric fabric tensor of unit norm and is also related to Lode angle of the fabric, $h_F$ ($0^\circ \le h_F \le 60^\circ$), through the following expression:

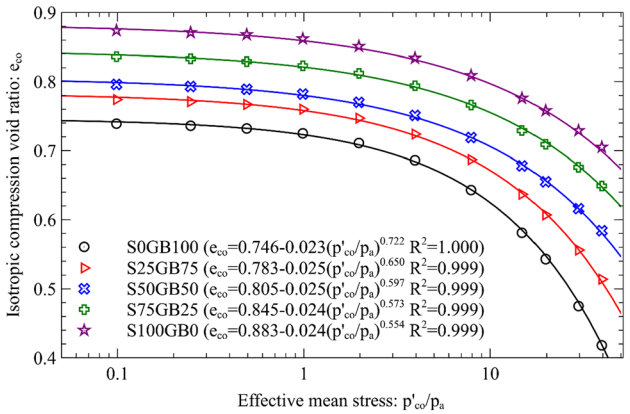


**Fig. 2** Isotropic compression void ratio for five uniformly graded granular samples with different ORs

$$\cos 3\theta_F = \sqrt{6}tr\mathbf{n}_F^3 \tag{14}$$

Note that a scaled $F$, $F'$ is generally used to quantify the fabric anisotropy of soils according to many studies [47, 48, 56]:

$$F' = \frac{15}{2}F \tag{15}$$

so that the orientation distribution probability density function $E(\theta)$ of contact normal $n$ in the global coordination system can be directly approximated by the second-order Fourier expansion of $E(\theta)$ as $E(\theta) = \frac{1}{4}(1 + F'_{ij}n_in_j)$ [34]. Hence, $F'$ is also adopted in this study for critical state anisotropic fabric analysis for the convenience of comparison with previous results.

## 3 Simulation results

In this section, the typical observed macro- and micro-mechanical responses of granular samples with different overall regularity, during numerical isotropic consolidation tests and triaxial compression tests under different drainage conditions, are presented. Note that since there is no standardized method to determine the relative density of the granular sample in DEM studies, hence all samples before shearing presented here are almost of the same density (but not the same relative density) and stress states in order to ensure the comparability. And the effect of particle overall regularity on the macro- and micro-mechanical behaviors of granular materials is further evaluated with critical state lines and critical state parameters in the subsequent section under the anisotropic critical state theory framework.

### 3.1 Isotropic compression tests

The isotropic compression tests are simulated with respect to five granular assemblies with varying overall regularities under a series of compression stress $p'_{co}$(= 10; 25; 50; 100; 200; 400; 800; 1500; 2000; 3000; 4000 kPa) During the isotropic compression process, the inter-particle friction coefficient is assigned with a typical value of quartz sand particles ($\mu = 0.3$) in order to investigate the influence of particle shape on the compression behavior of uniformly graded and sub-rounded sandy soils. Figure 2 presents the corresponding compression curves of $e_{co} - (p'_{co}/p_a)^{u_{co}}$ for these five assemblies; it can be seen that a nice exponential relationship, $e_{co} = e_{co0} - k_{co}(p'_{co}/p_a)^{u_{co}}$, is achieved from small confining stress and normal confining stress. And the isotropic compression void ratio of sands increases with the decrease in the overall regularity given a similar compression process. This indicates that irregular particles may provide more resistance to the relative rotation at particle corners and hence induce less particle rearrangement during compression and thus form a final relatively loose fabric structure within the soils. This effect is more serious for cases with a smaller *OR*. In addition, Fig. 3 gives the relations between the isotropic compression curve parameters and *OR*, and it is seen that the isotropic compression void ratio corresponding to a 'zero' effective mean stress $e_{co0}$ decreases, while the exponent $u_{co}$ increases linearly with the increasing of the OR. In addition, it is interesting to see that *OR* has a negligible effect on $k_{co}$(e.g., a very small coefficient of variation COV) within the studied range. These findings help in selecting constitutive parameters related to the compression behaviors of sands.

### 3.2 Triaxial compression tests

#### 3.2.1 Undrained shearing on samples with different ORs

The constant volume test simulations are conducted under the same initial state ($\sigma'_{3;0}$ = 100 kPa with $e_0$ about 0.76 except $e_0 = 0{:}73$ for S0GB100UD6) to investigate the undrained shearing behaviors of five types of granular samples with varying *OR*s. A slightly small initial void ratio for S0GB100 is used since it is unable to make a looser sample for this sample based on the adopted specimen preparation method. Figure 4 and Fig. 5 give the evolutions of deviatoric stress $q$, excess pore water pressure u and also the corresponding stress paths $q$-$p'$ of these samples during undrained shearing. It can be seen that these five granular samples with different overall regularities behave similarly with those of laboratory soils with different relative densities under undrained triaxial

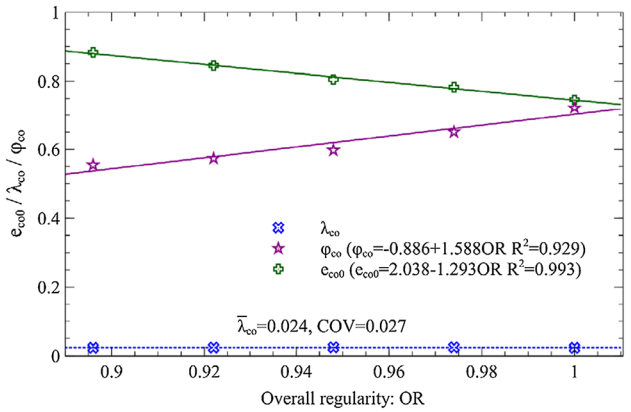


**Fig. 3** Relations between the isotropic compression curve parameters and OR

compression tests, respectively. Specifically, the responses of S0GB100UD6 and S25GB75UD6 samples represent the behaviors of loose sands. That is, the excess pore water pressure u increases continuously upon undrained shearing until reaching the initial effective mean stress and both the effective mean stress *p'* and deviatoric stress *q* decrease to zero, meaning that the static liquefaction phenomenon occurs within both samples. Note that the instability stress ratio of S25GB75UD6 is slightly larger than that of S0GB100UD6 although the density of the former before shearing is less than that of the latter, suggesting that particle shape has a noticeable effect on the soil response. In addition, an interesting observation is that during the static liquefaction, the shear strengths of these two samples are not strictly zero, which mainly results from the rearrangement of the constituent particles under the action of loading walls, and this phenomenon had also been reported in Gong et al. [15].

On the other hand, the other three types of samples with a smaller *OR* characterize with the undrained shearing responses of medium-dense, dense sands in the laboratory, respectively, among which both S75GB25UD6 and S100GB0UD6 samples experience a strain hardening process, and the deviatoric stress *q* of both samples increases quickly after loading until a critical state value. And both samples have the dilation tendency, and hence, the negative excess pore water pressure *u* increases with the shearing until reaching a steady value at the critical state. For the sample S50GB50UD6, the deviatoric stress *q* first increases to a peak value and then drops to a quasi-steady state. With further shearing, the volumetric deformation feature of the sample changes from contractive to dilative, and the positive excess pore water pressure *u* starts to decrease to the negative one constantly until a steady state, while the deviatoric stress increases continuously to a steady state. From the stress paths *q-p'* in Fig. 5(c), it can be easily seen that the peak and critical state undrained shear strength of

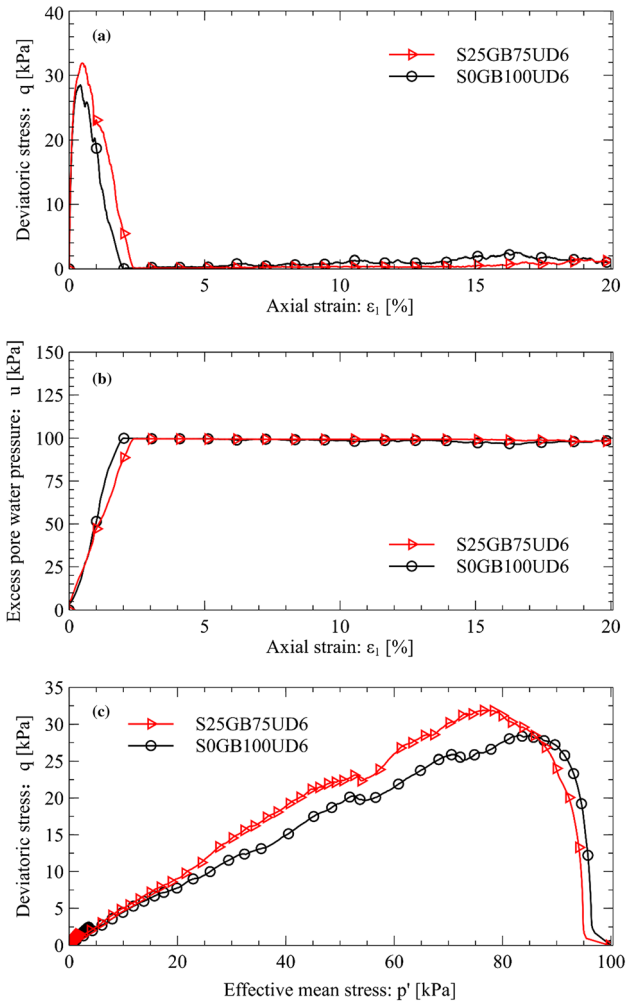


**Fig. 4** Evolutions of deviatoric stress q, excess pore water pressure *u*, and the stress path $q - p'$ for samples with different ORs during undrained shearing: S0GB100UD6 and S25GB75UD6

the granular sample with a same initial density decreases with the overall regularity.

On the microscopic scale, Fig. 6 gives the evolutions of mechanical coordination number $Z_m$ of these five samples during undrained shearing. It is obvious that the granular samples with different *ORs* have different evolutions of the mechanical coordination number during the undrained shearing. Although $Z_m$ has an instantaneous drop after loading within all samples, it will begin to increase in both S75GB25UD6 and S100GB0UD6 samples soon until reaching a steady value at the critical state. However, for the sample S50GB50UD6, the $Z_m$ first decreases to a minor value and then stays around this value for a short period, corresponding to the quasi-steady state. After that, it starts to increase with the axial strain until a steady value at the critical state. On the contrary, the $Z_m$ values in both S0GB100UD6 and S25GB75UD6 samples decrease quickly to a minimum less than the critical $Z_m$ (e.g., 4,

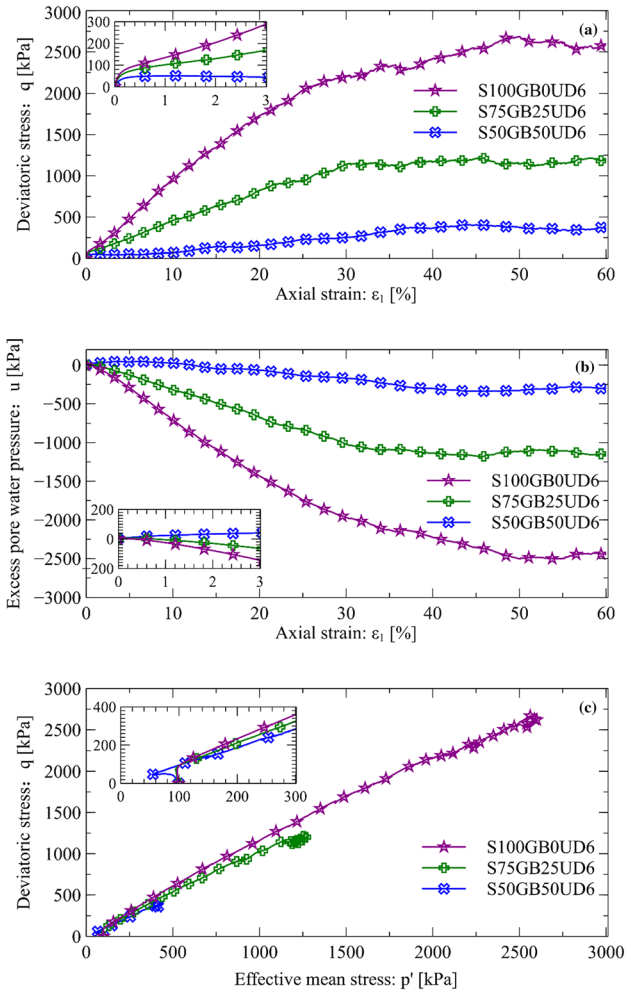


**Fig. 5** Evolutions of deviatoric stress q, excess pore water pressure u, and the stress path $q - p'$ for samples with different ORs during undrained shearing: S50GB50UD6, S75GB25UD6 and S100GB0UD6

[16]) ensuring the mechanical stability of sands, and then, static liquefaction occurs. With further loading, the $Z_m$ values in both samples have a slight rise but still lower than the initial values, and this is also the micro-mechanisms for which the effective stress in these two samples in Fig. 4 rises again after the static liquefaction. Moreover, comparing the $Z_m$ values between different samples, it can be concluded that the critical state $Z_m$ increases with the decrease in the *OR*.

Figure 7 presents the evolutions of the fabric norm $F$ and also the corresponding fabric Lode angle $\theta_F$ within these five types of granular assemblies. It can be seen that the contact normal-based fabric norm increases with the decrease in *OR*. Note that a not obvious 'softening' behavior is observed for the evolutions of $F$ within both S75GB25UD6 and S100GB0UD6 samples. This might due to a larger initial void ratio of 0.76, although their stress–strain characteristics are similar to those of dense sands in

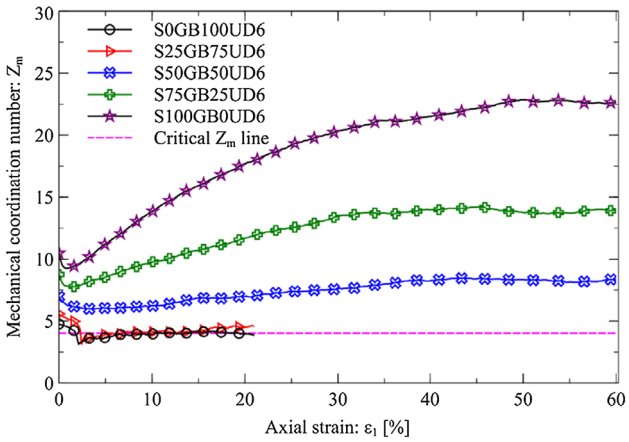


**Fig. 6** Evolutions of the mechanical coordination number $Z_m$ for five uniformly graded granular samples with different ORs during undrained shearing

the laboratory under the undrained condition. An obvious 'softening' behavior would be acquired for the same samples with a smaller initial void ratio, as shown in Fig. 10(a). For the fabric Lode angle $\theta_F$, a sharp reduction of $\theta_F$ is observed at the very beginning of loading (within the range of 2% axial strain) for all samples. And then it drops to a zero value, which means that the fabric direction within the sample is co-directional with the loading direction soon after shearing in order to withstand the external load better since the Lode angle of conventional triaxial loading mode is also zero.

### 3.2.2 Drained shearing on samples with different ORs

Similar to the constant volume tests, the drained shearing test simulations are also performed on five types of samples with different overall regularities under almost same initial stress and density state ($\sigma'_{3;0}$= 100 kPa and $e_0$ = 0.61 * 0.63). Figure 8 shows the evolutions of deviatoric stress $q$ and volume strain $\varepsilon_v$ with the axial strain $\varepsilon_1$. In Fig. 8(a), the deviatoric stress $q$ of all samples first increases to a peak value followed by a 'softening' behavior and then reach to a steady value at the critical state. In the meanwhile, all samples contract slightly upon shearing and then dilate significantly with further shearing, and a constant volume can be also seen at the critical state. Note that the peak and critical state shear strength and also the volume strain of the granular sample increase with the decrease in the *OR* under drained shearing.

Figure 9 gives the evolutions of the mechanical coordination number, $Z_m$, of these five samples under the drained condition. Different with the evolutions of $Z_m$ in the undrained condition, $Z_m$ within all these five samples decreases continuously until a steady value (e.g., larger than 4), and the critical state $Z_m$ increases with the decrease

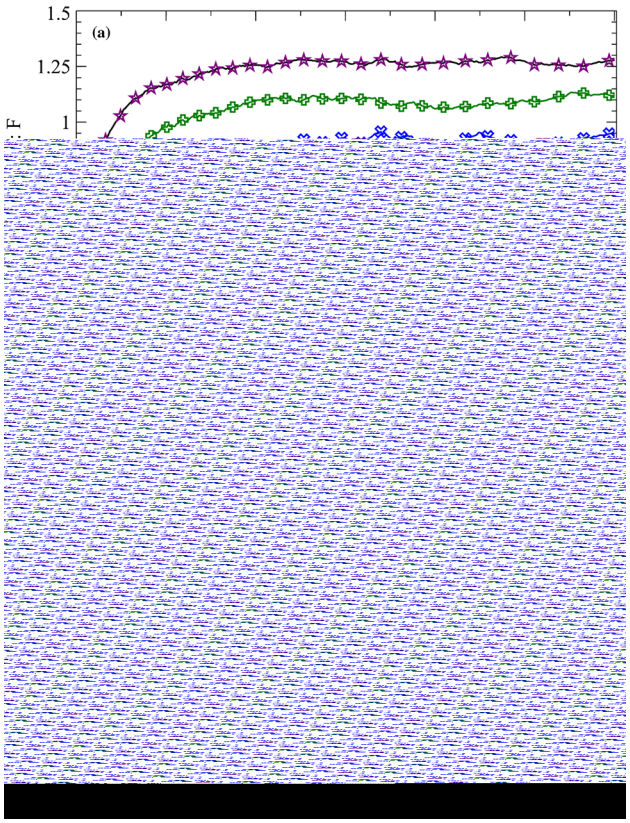


**Fig. 7** Evolutions of fabric norm F and fabric Lode angle $\theta_F$ for five uniformly graded samples with different ORs during undrained shearing

in the *OR*. Figure 10 illustrates the evolutions of fabric norm $F$ and also the corresponding fabric Lode angle $\theta_F$, which reflects the same result with that discussed for the undrained shearing condition in Fig. 7. And the presented fabric evolutions are also consistent with those of DEM simulations in Nguyen et al. [27, 28] and of experimental results in Zhao et al. [55] for dense sands. In order to discuss whether there exists a unique contact normal-based fabric norm when sandy soils reach to the critical state, Fig. 11 presents the critical state fabric norm $F_c$ of the five assemblies with varying *OR* under different initial states and drained conditions. It is seen that except for the pure sphere assembly S0GB100, $F_c$ of all other assemblies reach to constant values with negligible scatterings (e.g., a very small COV), and the magnitude of $F_c$ depends on the particle shape and decreases with the particle overall regularity. This interesting observation is somewhat different from those observed in Xie et al. [47] and Jiang et al. [18], which presented that the critical state fabric norm $F_c$ of sphere or elongated clump specimens increased with the increase of critical state void ratio. This difference may have been caused by neglecting the realistic shape characteristics (e.g., shape poly-dispersity, concave and convex features) in these studies. Hence, it seems that the uniqueness of critical state fabric norm based on contact normal is attainable for realistic shape particles but not for simple regular or convex particles. This observation,

**Fig. 8** Evolutions of deviatoric stress q and volume strain $\varepsilon_v$ for five uniformly graded samples with different ORs during drained shearing

**Fig. 9** Evolutions of the mechanical coordination number $Z_m$ for five uniformly graded samples with different ORs during drained shearing